materials

MDPI

Article

The Influence of a Binder in a Composite Electrode: The Case Study of Vanadyl Phosphate in Aqueous Electrolyte

Dragana Jugović [1,*], Miloš D. Milović [1,*], Tanja Barudžija [2], Maja Kuzmanović [1], Milica Vujković [3] and Miodrag Mitrić [2]

[1] Institute of Technical Sciences of SASA, 11000 Belgrade, Serbia
[2] "VINČA" Institute of Nuclear Sciences—National Institute of the Republic of Serbia, University of Belgrade, 11000 Belgrade, Serbia
[3] Faculty of Physical Chemistry, University of Belgrade, 11000 Belgrade, Serbia
* Correspondence: dragana.jugovic@itn.sanu.ac.rs (D.J.); milos.milovic@itn.sanu.ac.rs (M.D.M.)

Abstract: Layered $VOPO_4 \cdot 2H_2O$ is synthesized by the sonochemical method. An X-ray powder diffraction is used to examine the crystal structure, while scanning electron microscopy is used to reveal the morphology of the powder. The crystal structure refinement is performed in the P4/*nmm*Z space group. The electrochemical intercalation of several cations (Na^+, Mg^{2+}, Ca^{2+}, and Al^{3+}) in saturated nitrate aqueous solutions is investigated. The most notable reversible activity is found for the cycling in aluminium nitrate aqueous solution in the voltage range from −0.1 to 0.8 V vs. SCE. During the preparation of the electrode, it is observed that the structure is prone to changes that have not been recorded in the literature so far. Namely, the use of conventional binder PVDF in NMP solution deteriorates the structure and lowers the powder's crystallinity, while the use of Nafion solution causes the rearrangement of the atoms in a new crystal form that can be described in the monoclinic $P2_1/c$ space group. Consequently, these structural changes affect electrochemical performances. The observed differences in electrochemical performances are a result of structural rearrangements.

Keywords: $VOPO_4 \cdot 2H_2O$; aqueous batteries; binder; crystal structure refinement; electrochemical properties

Citation: Jugović, D.; Milović, M.D.; Barudžija, T.; Kuzmanović, M.; Vujković, M.; Mitrić, M. The Influence of a Binder in a Composite Electrode: The Case Study of Vanadyl Phosphate in Aqueous Electrolyte. *Materials* **2022**, *15*, 9041. https://doi.org/10.3390/ma15249041

Academic Editor: Ricardo Alcántara

Received: 27 October 2022
Accepted: 13 December 2022
Published: 17 December 2022

1. Introduction

The development of safe, durable, cheap, and environmentally friendly batteries is one of the most important challenges of modern electrochemistry. Hence, there is an interest in the research of aqueous multivalent ion batteries, such as calcium, magnesium, and aluminium aqueous batteries [1,2]. $VOPO_4 \cdot 2H_2O$, with its layered structure, is a particularly interesting and promising material for cation intercalation [3–13]. Vanadium V^{5+} ion can be reduced to a +3-oxidation state, opening up the possibility of more than one electron reaction per transition metal. The layered structure of $VOPO_4 \cdot 2H_2O$ can intercalate various species (molecules or ions) that cause a change in the interlayer distance [14–16] or/and the exfoliation of the bulk structure into 2D sheets [3,14,17]. Various cations can intercalate within the $VOPO_4 \cdot 2H_2O$ structure by redox reactions in iodide solutions [18–20]. However, there are few reports on the electrochemical intercalation of different cations in aqueous electrolytes. Literature data mainly report the electrochemical intercalation of zinc [3,12,21–24] and aluminium ions [7,11] in aqueous electrolytes. The electrochemical measurements use a composite electrode comprising active mass particles, conductive additives, and a polymeric binder. Binders have an important effect on the performance of the cell by maintaining both the mechanical and electrical integrity of the electrode network [25]. However, the presence of a binder may influence the properties of the materials under examination to an unknown extent [26]. Poly(vinylidene fluoride) (PVDF) dissolved in N-methyl-2-pyrrolidone (NMP) is the most commonly used binder solution [27]. Due to

both economic and healthcare issues connected to NMP, there is a need for less expensive and less hazardous aqueous-based solvents [28]. For that reason, another frequently used binder is Nafion (a sulfonated tetrafluoroethylene-based fluoropolymer-copolymer), which dissolves in aqueous-based solvents.

This work reports the electrochemical intercalation of several cations (Na^+, Mg^{2+}, Ca^{2+}, and Al^{3+}) in saturated nitrate aqueous solutions in sonochemically derived $VOPO_4 \cdot 2H_2O$. The working electrodes were prepared with PVDF or Nafion as a binder. It is revealed that, regardless of the choice of the binder, aluminium exhibits the most notable electrochemical activity among other ions, holding promise for its potential application in aqueous batteries. An interesting observation was made, namely that the application of the binder influences the structure of the active material, something that has not been reported in the literature for vanadyl phosphate.

2. Materials and Methods

The sonochemical method was used for the synthesis of the $VOPO_4 \cdot 2H_2O$ powder. By following the experimental data given in ref. [10], the synthesis was performed within a short time. A high-intensity ultrasonic probe of 750 W (Vibracell sonicator VCX 750, Sonics & Materials Inc., Newtown, CT, USA) that operates at 20 kHz with a 13 mm Ti-alloy probe was used to sonicate the reaction mixture. The reaction mixture, consisting of 1 g of V_2O_5, 15.8 mL of 85% H_3PO_4, and 100 mL of water, was introduced to the ultrasound irradiation under ambient air for 20 min while working in a pulsed mode: 1 s with an ultrasound on followed by a rest for 1 s. The obtained yellow powder was washed with water and acetone and dried at 100 °C.

X-ray powder diffraction was performed on a Philips PW 1050 diffractometer (Amsterdam, The Netherlands) with Cu–K$\alpha_{1,2}$ radiation (Ni filter) at room temperature. The diffraction data were collected in two manners: a scanning step width of 0.05° and 3 s time per step in a 2θ range of 10–70° and a scanning step width of 0.02° and 14 s per step in the 2θ range from 10–110° were applied for phase identification and for the crystal structure refinement, respectively.

SEM analysis was performed on a Mira XMU TESCAN electron microscope (Kohoutovice, Czech Republic).

The FTIR spectra of the samples were recorded at ambient conditions in the mid-IR region (400–4000 cm^{-1}) with a Nicolet IS 50 FT-IR spectrometer (Waltham, MA, USA) operating in the ATR mode with a measuring resolution of 4 cm^{-1} and 32 scans.

The electrochemical measurements were conducted by using Vertex.One potentiostat/galvanostat (Ivium Technologies, Eindhoven, The Netherlands). The measurements were performed using four different aqueous electrolytes (saturated aqueous solutions of $Al(NO_3)_3$, $Ca(NO_3)_2$, $NaNO_3$, and $Mg(NO_3)_2$). The working electrode was made from a slurry of active material, carbon black PBX51 (Cabot Corp., Boston, MA, USA), and a binder (PVDF, 2.4 wt% solution in N-methyl-2-pyrroliperformed or Nafion, 5 wt% solution in a mixture of lower aliphatic alcohols and water) mixed in a weight ratio of 70:20:10, respectively. The slurry was deposited on glassy carbon and then dried at 120 °C. Cyclic voltammetry (CV) measurements were performed in a three-electrode cell with platinum as a counter electrode and SCE (saturated calomel electrode; SI Analytics, Mainz, Germany) as a reference electrode. Galvanostatic measurement was performed in a two-electrode cell with glassy carbon as a counter electrode. Electrochemical impedance spectroscopy (EIS) measurements were performed within the frequency range of 10^5 to 10^{-2} Hz with a perturbation amplitude of 5 mV. The impedance spectra were recorded at the potential of the cathodic peak at the CV curve.

3. Results and Discussion

3.1. The Structure and Morphology

X-ray powder diffraction data were used for both phase check and crystal structure refinement. The structure of the powder was refined in the tetragonal space group P4/*nmm*Z

(No. 129) with the following crystallographic positions: vanadium ions occupy 2*c* [$\frac{1}{4}$, $\frac{1}{4}$, z] octahedral crystallographic position; phosphorus ions are located at a tetrahedral position 2b [$\frac{3}{4}$, $\frac{1}{4}$, $\frac{1}{2}$]; there are four different crystallographic positions where oxygen ions are allocated: additional two 2c positions (denoted as O2 and O4), one 8i [$\frac{1}{4}$, y, z] position (denoted as O1), and 2a [$\frac{3}{4}$, $\frac{1}{4}$, 0] crystallographic position (denoted as O3). Crystal structure refinement was based on the Rietveld full-profile method [29] using the Koalariet computing program, based on the fundamental parameters convolution approach in diffraction line profile fitting [30].

The structure (Figure 1) can be illustrated by infinite layers of VO_6 octahedra connected to the PO_4 tetrahedra. Within the layer, each VO_6 octahedron is corner-connected to four PO_4 tetrahedra via its equatorial oxygen ions (O1 site) in a zig-zag manner. Namely, the VO_6 octahedron is distorted along the *c* axis and its apical oxygen ions (O2 and O4) alternate up and down relative to the layer. The water molecules are located between two layers. The interslab distance varies with the content of interlayered water. There are two kinds of water molecules (Figure 1): structural water, which is directly bonded to vanadium ion (at the O2 site), and crystal water, which is located between two VPO layers and contains oxygen O3 that belongs neither to VO_6 octahedron nor PO_4 tetrahedron [13,31]. The second water molecule forms hydrogen bonds with two PO_4 groups of different layers [31]. The results of the refinement are given in Tables 1 and 2, while its graphical representation is given in Figure 2. The lattice parameters (*a* = 6.214, *b* = 6.214, and *c* = 7.414 Å) are in good agreement with the literature data [10,13,28]. The value of the *c* parameter implies that the structure has two water molecules per formula unit [32]. Both refined and fixed fractional atomic coordinates were used to calculate all relevant bond distances given in Table 3. A significantly shorter V–O4 bond implies the presence of the $[V{=}O]^{3+}$ cation [33].

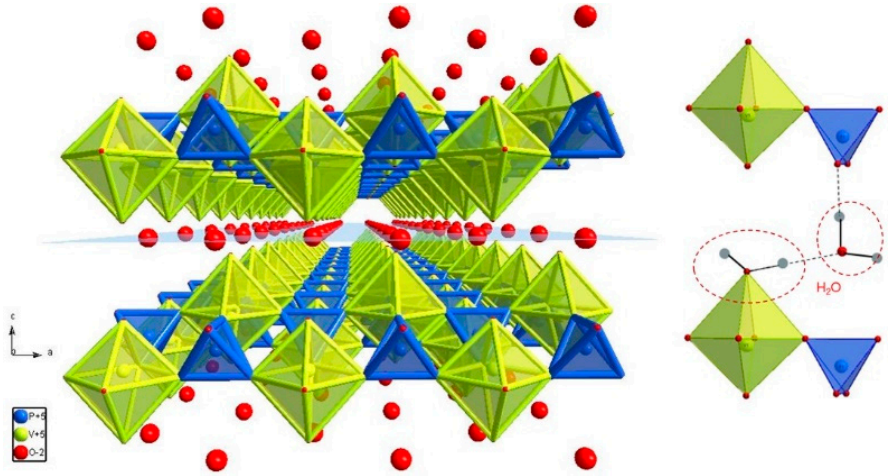

Figure 1. The polyhedral illustration of the structure of the $VOPO_4{\cdot}2H_2O$ created by the molecular and crystal structure visualization software Diamond 3.2 (**left**); the positions of water molecules (**right**).

Table 1. The main results of the refinement in the space group P4/*nmm*Z.

Lattice parameters (Å)	a = 6.2138 (9) b = 6.2138 (9) c = 7.4140 (10)
Primitive cell volume (Å^3)	V = 286.26 (9)
Mean crystallite size (nm)	280 (20)
Microstrain (%)	0.38 (2)

Table 2. Fixed and refined fractional atomic coordinates.

Fractional Coordinates	x	y	z	B [Å^2]
P1 (2b)	0.75	0.25	0.5	2.5
V (2*c*)	0.25	0.25	0.4092 (5)	0.5
O1 (8*i*)	0.25	0.941 (2)	0.3809 (8)	0.4
O2 (2*c*)	0.25	0.25	0.091 (2)	2.1
O3 (2*a*)	0.75	0.25	0	2.1
O4 (2*c*)	0.25	0.25	0.631 (1)	2.1

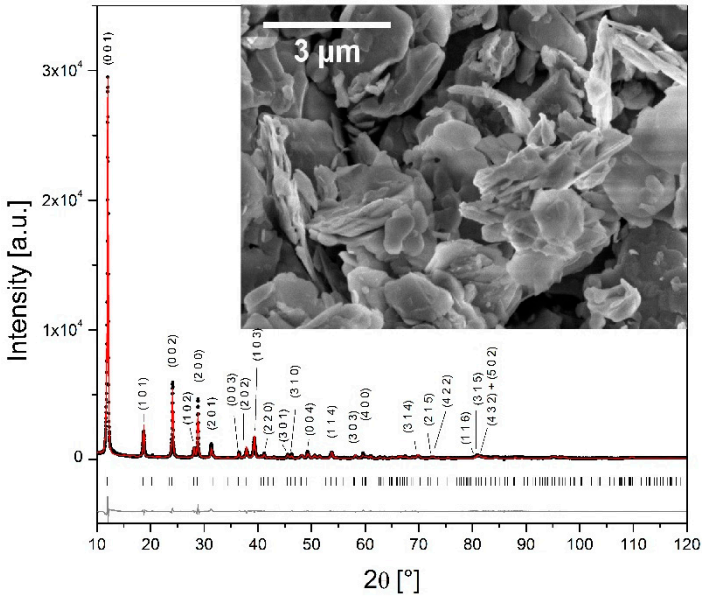

Figure 2. The observed (·), calculated (-), and the difference between the observed and calculated (bottom) X-ray diffraction data taken at room temperature of $VOPO_4 \cdot 2H_2O$ powder. Vertical markers below the diffraction patterns indicate the positions of possible Bragg reflections. Inset: SEM micrograph of $VOPO_4 \cdot 2H_2O$ powder.

Table 3. Selected bond distances and polyhedral distortions.

M–O Bond	Bond Length [Å]
P–O1 × 4	1.4804 (97)
P–O3 × 2	3.7070 (5)
(P–O1) $_{aver.}$	1.4804 (97)
PO_4 distortion	0
V–O1 × 4	1.930 (11)
V–O2	2.357 (13)
V–O4	1.644 (11)
(V–O) $_{aver.}$	1.954
VO_6 distortion	1.1×10^{-2}

SEM micrographs reveal platelet morphology (inset of Figure 2). Micron-sized particles show the lamellar assembly typical for layered structures.

The FTIR spectrum of the as-synthesized powder (Figure 3) shows characteristic bands for $VOPO_4 \cdot 2H_2O$ [31]. Absorption bands that correspond to V-O and P-O stretching appear between 1200 and 600 cm^{-1}, while O–V–O and O–P–O bending modes can be observed below 600 cm^{-1} [6,19]. The stretching O–H modes of water molecules can be seen from 3300 to 3600 cm^{-1}, and bending bands are seen around 1600 cm^{-1}. In the hydroxyl-stretching region, two observed bands can be assigned to two types of water molecules. The sharp one

at 3600 cm^{-1} corresponds to the lattice water molecule, which is bound to the vanadium, while the hump at 3330 cm^{-1} is ascribed to the interlayer water molecule, which is not fully hydrogen-bonded and therefore less tightly bonded [31,33].

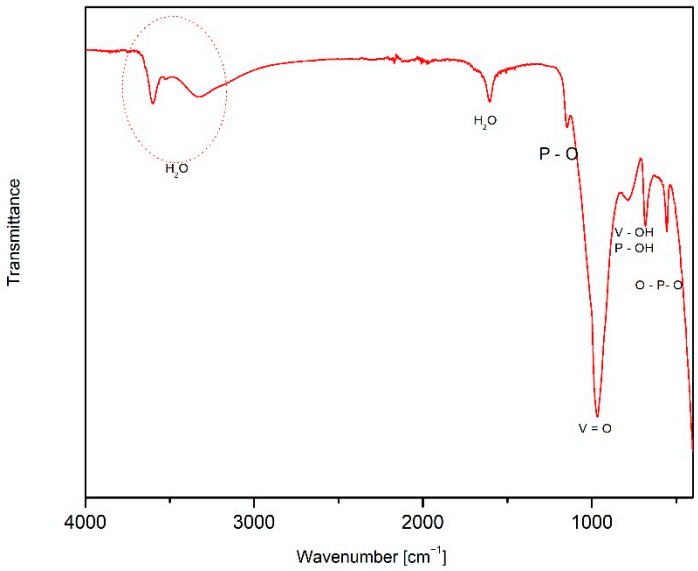

Figure 3. FTIR spectrum of the $VOPO_4 \cdot 2H_2O$.

3.2. Behind the Scenes of Electrode Preparation

The electrochemical measurements are performed with the composite electrode comprising active mass particles, conductive additives, and a polymeric binder. Since there were indices that the active material, $VOPO_4 \cdot 2H_2O$, is prone to a change, the electrode's preparation procedure was followed step by step by both X-ray diffraction and FT-IR measurements. X-ray patterns (Figure 4a) imply that the structure of the $VOPO_4 \cdot 2H_2O$ powder is stable on grinding in a mortar, drying at 120 °C, and ageing in the air for 7 months. However, mixing the $VOPO_4 \cdot 2H_2O$ with carbon black causes the appearance of new 2θ peaks at around 12.40°, 25°, and 29.44° in close proximity to the 001, 002, and 200 reflections, respectively (Figure 4b).

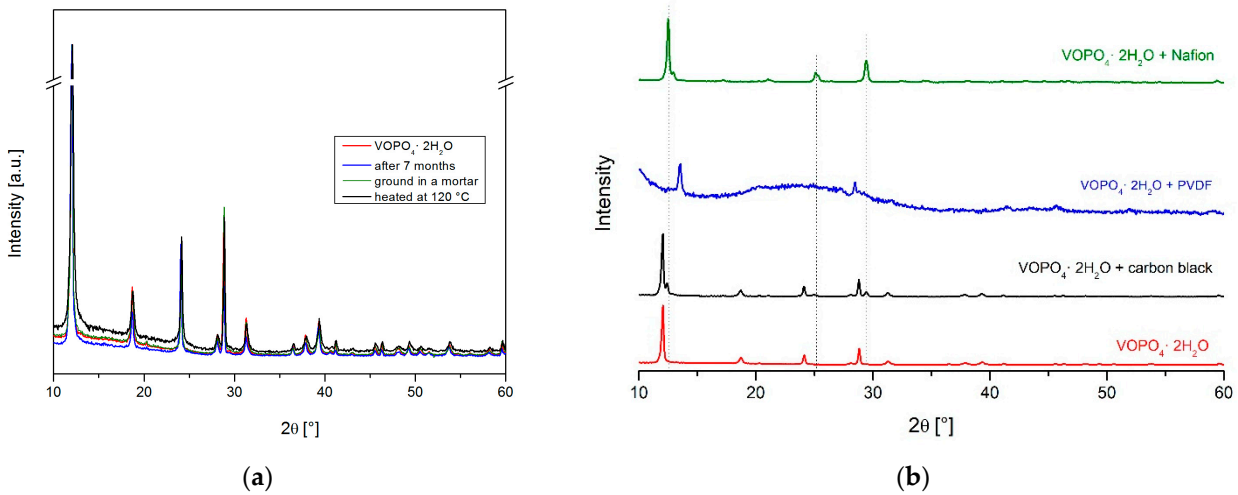

Figure 4. (**a**) XRD patterns of the $VOPO_4 \cdot 2H_2O$ powder after grinding in a mortar, drying at 120 °C, and ageing in the air for 7 months; (**b**) Comparison of the XRD patterns of the $VOPO_4 \cdot 2H_2O$ powder, its mixtures with carbon black (PBX51), and carbon black and a binder (PVDF or Nafion).

These peaks can be attributed to a new phase of the smaller *c* parameter, probably formed as a consequence of the partial loss of the intercalated water due to the hydrophilic nature of carbon additive (PBX51). On further addition of the dissolved PVDF in NMP to the mixture of the $VOPO_4 \cdot 2H_2O$ and carbon black, an abrupt disorder of the material's structure can be noticed. Additional X-ray diffraction measurements of the mixture with NMP solvent alone showed that essentially NMP is responsible for the collapse of the structure due to its polarity and surface tension. The mechanism most probably follows the scheme for graphite exfoliation [34]; however, this time, the penetration of NMP between layers of $VOPO_4 \cdot 2H_2O$ causes the breakage of hydrogen bonding between crystal water and lattice oxygen, resulting in part of the water molecules leaving the structure. This gives rise to an X-ray pattern with very few peaks of much lower intensities, indicating both the decrease in crystallinity and the severe preferred orientation. Additionally, the swelling/exfoliation process cannot be ruled out [35]. A shift in the most intense peak to a higher angle implies a decrease in the interlayer distance (around 5.8 Å). In addition, FTIR measurements confirmed both the partial loss of water molecules and the presence of NMP molecules. Another binder was utilized, Nafion 5 wt% solution in a mixture of lower aliphatic alcohols and water. It turned out that the Nafion solution also alters the pristine structure (Figure 4b), but in a different way. This time, well-defined, intense new peaks are observed, while the peaks of the pristine structure, $VOPO_4 \cdot 2H_2O$, completely vanished. This new pattern entirely matches the pattern of the $H_xVOPO_4 \cdot 2.33H_2O$ phase, which has a partly reduced vanadium and whose structure can be described in the $P2_1/c$ monoclinic space group [35]. The lattice parameters of the new monoclinic phase are obtained by Le Bail fit [36,37] and amount to a = 7.4, b = 26.4, and c = 8.8 Å with an angle β = 106.6°. They are related to the lattice parameters of the pristine tetragonal phase by the equations $b_m = \sqrt{2} \cdot 3a_t$ and $c_m = \sqrt{2}a_t$ (where t and m refer to the tetragonal and monoclinic phases, respectively). These findings are in agreement with the results of Shpeizer et al. [35], who first reported the existence of this phase. Previously mentioned additional peaks that emerged in the XRD pattern of the mixture comprising $VOPO_4 \cdot 2H_2O$ and carbon black can be indexed as belonging to this reduced phase. To the best of our knowledge, none of the papers in the literature report similar phenomena.

Figure 5 shows continuous changes in the band features of the infrared spectra. The bands attributed to water molecules (at 3600, 3300, and 1600 cm^{-1}) decrease in intensity, even after mixing the pristine powder with carbon black. This is associated with lattice water expulsion, as assumed in the XRD analysis. The addition of a binder solution to this mixture causes a profound intensity decrease in the water bands (when Nafion is a binder) or their full disappearance (when PVDF is a binder). The spectrum of the PVDF-containing mixture underwent the greatest changes, with the bands of the parent phase subsiding while the new bands rise. These bands correspond to NMP [38], which can be interpreted as pyrrolidone being incorporated into the crystal structure, most likely as a partial replacement of the water molecules in the interlayer space. Bands that correspond to the vibration of the PO_4 group are slightly red-shifted, implying bond elongation due to a replacement of water molecules with solvent molecules.

3.3. Electrochemical Properties

Cyclic voltammetry measurements were used to study the electrochemical response of $VOPO_4 \cdot 2H_2O$ in various aqueous electrolytes, as displayed in Figure 6. Figure 6a presents the cyclic voltammograms (CV) at a 10 mVs^{-1} scan rate of an electrode immersed in $NaNO_3$, $Ca(NO_3)_2$, $Mg(NO_3)_2$, and $Al(NO_3)_3$ solutions. An interesting feature is that the CV curves profiles vary not only by the variation of electrolyte but also with the binder used in electrode preparation. It can be noticed that the best electrochemical response was obtained when the cycling was performed in an aluminium nitrate solution.

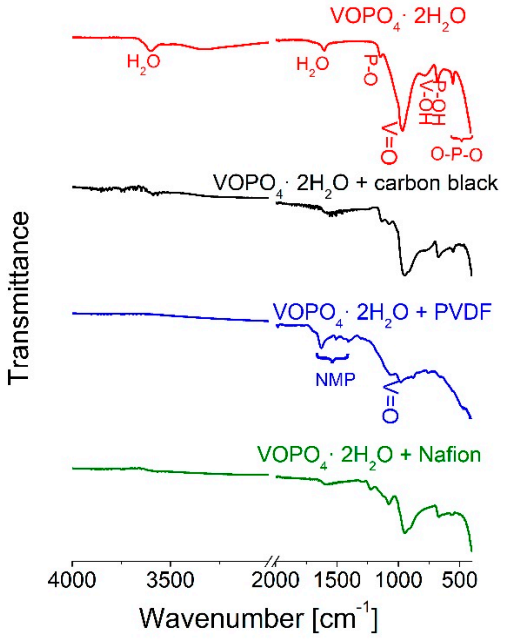

Figure 5. Comparison of FTIR spectra of the $VOPO_4 \cdot 2H_2O$ and its mixtures with carbon black, carbon black and PVDF, and carbon black and Nafion.

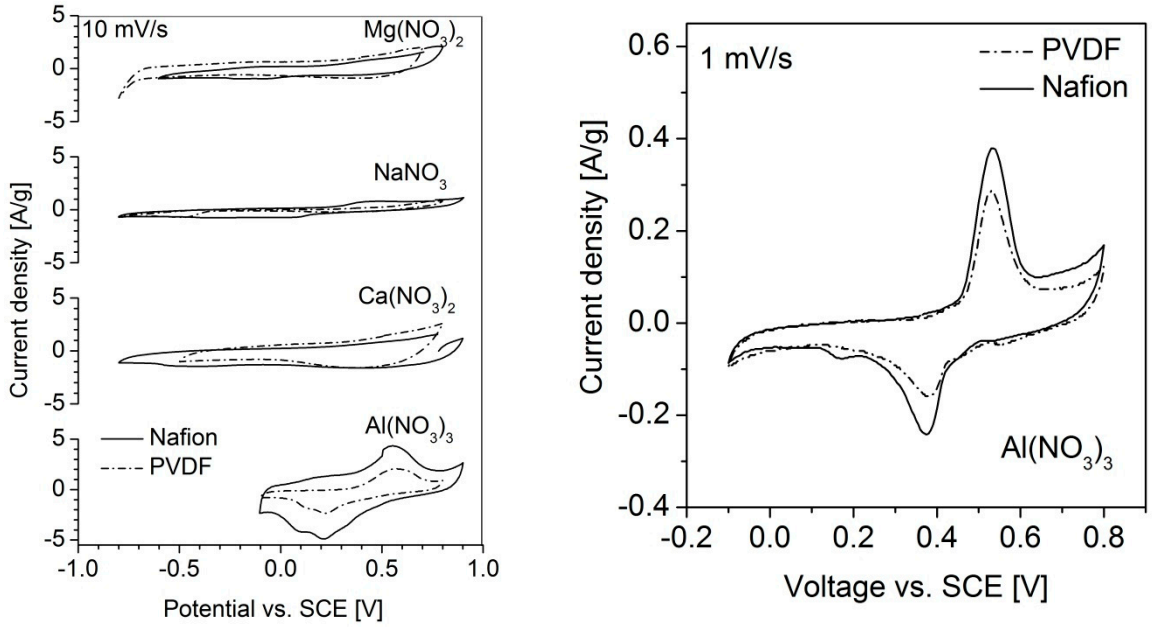

(**a**) (**b**)

Figure 6. (**a**) Cyclic voltammograms of the composite electrode comprising $VOPO_4 \cdot 2H_2O$, carbon black, and a binder (PVDF or Nafion) in $NaNO_3$-, $Ca(NO_3)_2$-, $Mg(NO_3)_2$-, and $Al(NO_3)_3$-saturated aqueous solutions at scan rate of 10 mVs^{-1}. (**b**) Cyclic voltammograms of the composite electrode comprising $VOPO_4 \cdot 2H_2O$, carbon black, and a binder (PVDF or Nafion) in $Al(NO_3)_3$-saturated aqueous solution at scan rate of 1 mVs^{-1}.

The cyclic voltammograms obtained in the $Al(NO_3)_3$ solution are characterized by a larger enclosed area and fairly defined redox peaks of higher current intensities. These peaks are more pronounced at a lower scan rate (Figure 6b) and can be ascribed to V^{+5}/V^{+4} redox reactions on the basis of their position (~0.5 V vs. SCE) [39]. Galvanostatic charge–discharge tests in $Al(NO_3)_3$ solution are shown in Figure 7a. The continuous sloping curve

profile indicates a homogeneous distribution of aluminium ions within the structure of the active material applied with PVDF binder. On the other hand, the stepped curve of the active material applied with Nafion binder indicates the structural transition of the host, i.e., possible changes in the crystallographic environment of vanadium and/or aluminium ion positions with consequent alternation of insertion/extraction voltage. However, for both electrodes (with PVDF or Nafion), the obtained capacity is smaller than the theoretical one, suggesting the sluggish charge transfer kinetics of the electrode.

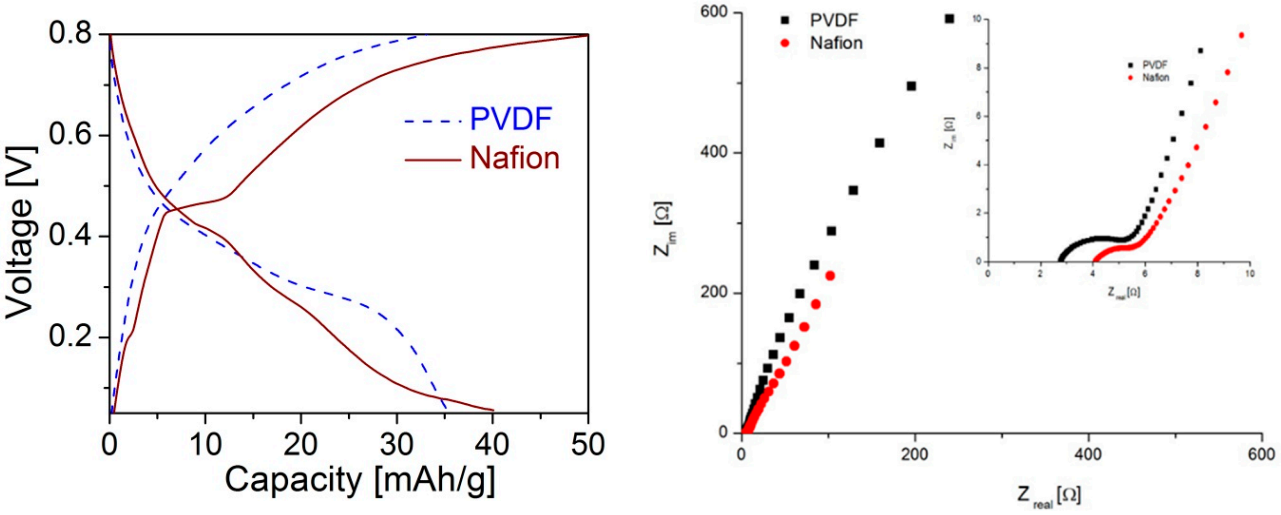

(**a**) (**b**)

Figure 7. (**a**) Galvanostatic curves obtained for the composite electrodes comprising $VOPO_4 \cdot 2H_2O$, carbon black, and a binder (PVDF or Nafion) in $Al(NO_3)_3$ saturated aqueous solution; applied current: 20 mA/g. (**b**) The corresponding Nyquist plots for two cells with these electrodes. The inset is enlarged high-frequency region.

Electrochemical impedance spectroscopy plots of the cells with $Al(NO_3)_3$-saturated aqueous solution (Figure 7b) are composed of a depressed semicircle at high frequencies (inset of Figure 7b), followed by an inclined line. The smaller radius of the semi-circle noticed for an electrode made with Nafion implies smaller charge transfer resistance. The structural changes created during the electrode's preparation with Nafion binder alleviate charge transfer.

In contrast to $Al(NO_3)_3$, the CV curves (Figure 6a) recorded in the other three electrolytes ($NaNO_3$, $Ca(NO_3)_2$, and $Mg(NO_3)_2$) exhibit quasi-rectangular shapes with broad peaks and large polarization, implying pseudocapacitive behaviour without noticeable redox activity. This can be interpreted that in the case of $NaNO_3$, $Ca(NO_3)_2$, or $Mg(NO_3)_2$ electrolytes there are no intercalation reactions of a certain cation (Na^+, Ca^{2+}, or Mg^{2+}) within the structure. Various factors related to the structure and to the electrolytes can be a cause of such differences, for example, the difference in the ionic radii of the cations [40], the pH value of the electrolytes, ionic conductivity, and the viscosity of the electrolyte [41,42].

4. Conclusions

$VOPO_4 \cdot 2H_2O$, synthesized by the sonochemical method, was investigated as a cathode material in aqueous cells. The crystal structure refinement confirmed crystallization in the P4/*nmm*Z space group. The structure of the synthesized powder is stable upon ageing in air, grinding in a mortar, and heating to 120 °C. During the preparation of the electrode, it was found that the binder influences the structure of the active material, which has not been recorded in the literature so far. Namely, the use of a conventional binder PVDF in NMP solution degrades the structure and lowers its crystallinity, while the use of Nafion solution causes the rearrangement of the atoms in a new crystal form that can be described

as a monoclinic $P2_1/c$ space group. The cycling voltammetry measurements evidenced electrochemical activity with a pronounced V^{5+}/V^{4+} redox pair in $Al(NO_3)_3$ solution, regardless of the binder used. In contrast, CV curves recorded in $NaNO_3$, $Ca(NO_3)_2$, and $Mg(NO_3)_2$ solutions exhibited quasirectangular shapes, implying pseudocapacitive behaviour. The study reveals new insights in the relation between binder and active material, often considered as mutually non-interacting.

Author Contributions: D.J.: conceptualization, investigation, methodology, writing—original draft; M.D.M.: conceptualization, investigation, methodology, writing—original draft; T.B.: investigation; M.K.: investigation; M.V.: investigation; M.M.: supervision, writing—reviewing and editing. All authors have read and agreed to the published version of the manuscript.

Funding: This work was financially supported by the Ministry of Education, Science and Technological Development of the Republic of Serbia, through agreements related to the realization and financing of scientific research work of the Institute of Technical Sciences of SASA (Contract No. 451-03-68/2022-14/200175), and by the Science Fund of the Republic of Serbia, PROMIS, #6062667, HISUPERBAT.

Institutional Review Board Statement: Not applicable.

Informed Consent Statement: Not applicable.

Data Availability Statement: The raw data required to reproduce these findings cannot be shared at this time as the data also form part of an ongoing study.

Conflicts of Interest: The authors declare no conflict of interest.

References

1. Liu, J.; Xu, C.; Chen, Z.; Ni, S.; Shen, Z.X. Progress in Aqueous Rechargeable Batteries. *Green Energy Environ.* **2018**, *3*, 20–41. [CrossRef]
2. Yuan, X.; Ma, F.; Zuo, L.; Wang, J.; Yu, N.; Chen, Y.; Zhu, Y.; Huang, Q.; Holze, R.; Wu, Y.; et al. *Latest Advances in High-Voltage and High-Energy-Density Aqueous Rechargeable Batteries*; Springer: Singapore, 2021; Volume 4, ISBN 0123456789.
3. Wu, Z.; Lu, C.; Ye, F.; Zhang, L.; Jiang, L.; Liu, Q.; Dong, H.; Sun, Z.; Hu, L. Bilayered $VOPO_4{\cdot}2H_2O$ Nanosheets with High-Concentration Oxygen Vacancies for High-Performance Aqueous Zinc-Ion Batteries. *Adv. Funct. Mater.* **2021**, *31*, 2106816. [CrossRef]
4. Dupré, N.; Gaubicher, J.; Le Mercier, T.; Wallez, G.; Angenault, J.; Quarton, M. Positive Electrode Materials for Lithium Batteries Based on $VOPO_4$. *Solid State Ion.* **2001**, *140*, 209–221. [CrossRef]
5. Zhang, Z.; Ni, Y.; Avdeev, M.; Kan, W.H.; He, G. Dual-Ion Intercalation to Enable High-Capacity $VOPO_4$ Cathodes for Na-Ion Batteries. *Electrochim. Acta* **2021**, *365*, 137376. [CrossRef]
6. Zhang, X.; Yang, D.; Liu, W.; Rui, X. $VOPO_4{\cdot}2H_2O$: Large-Scale Synthesis and Zinc-Ion Storage Application. *Front. Energy Res.* **2020**, *8*, 211. [CrossRef]
7. Pang, Q.; Yang, S.; Yu, X.; He, W.; Zhang, S.; Tian, Y.; Xing, M.; Fu, Y.; Luo, X. Realizing Reversible Storage of Trivalent Aluminium Ions Using $VOPO_4{\cdot}2H_2O$ nanosheets as cathode material in aqueous aluminum metal batteries. *J. Alloys Compd.* **2021**, *885*, 161008. [CrossRef]
8. Wang, J.; Tan, S.; Xiong, F.; Yu, R.; Wu, P.; Cui, L.; An, Q. $VOPO_4{\cdot}2H_2O$ as a New Cathode Material for Rechargeable Ca-Ion Batteries. *Chem. Commun.* **2020**, *56*, 3805–3808. [CrossRef]
9. Verma, V.; Kumar, S.; Manalastas, W.; Zhao, J.; Chua, R.; Meng, S.; Kidkhunthod, P.; Srinivasan, M. Layered $VOPO_4$ as a Cathode Material for Rechargeable Zinc-Ion Battery: Effect of Polypyrrole Intercalation in the Host and Water Concentration in the Electrolyte. *ACS Appl. Energy Mater.* **2019**, *2*, 8667–8674. [CrossRef]
10. Park, N.G.; Kim, K.M.; Chang, S.H. Sonochemical Synthesis of the High Energy Density Cathode Material $VOPO_4{\cdot}2H_2O$. *Electrochem. Commun.* **2001**, *3*, 553–556. [CrossRef]
11. Wang, P.; Chen, Z.; Wang, H.; Ji, Z.; Feng, Y.; Wang, J.; Liu, J.; Hu, M.; Fei, J.; Gan, W.; et al. A High-Performance Flexible Aqueous Al Ion Rechargeable Battery with Long Cycle Life. *Energy Storage Mater.* **2020**, *25*, 426–435. [CrossRef]
12. Shi, H.; Song, Y.; Qin, Z.; Li, C.; Guo, D.; Liu, X.; Sun, X. Inhibiting $VOPO_4{\cdot}X\,H_2O$ Decomposition and Dissolution in Rechargeable Aqueous Zinc Batteries to Promote Voltage and Capacity Stabilities. *Angew. Chem.* **2019**, *131*, 16203–16207. [CrossRef]
13. Hyoung, J.; Heo, J.W.; Chae, M.S.; Hong, S.T. Electrochemical Exchange Reaction Mechanism and the Role of Additive Water to Stabilize the Structure of $VOPO_4{\cdot}2H_2O$ as a Cathode Material for Potassium-Ion Batteries. *ChemSusChem* **2019**, *12*, 1069–1075. [CrossRef] [PubMed]
14. Wu, C.; Lu, X.; Peng, L.; Xu, K.; Peng, X.; Huang, J.; Yu, G.; Xie, Y. Two-Dimensional Vanadyl Phosphate Ultrathin Nanosheets for High Energy Density and Flexible Pseudocapacitors. *Nat. Commun.* **2013**, *4*, 2431. [CrossRef] [PubMed]

15. Sithamparappillai, U.; Nuño, J.L.; Dummer, N.F.; Weng, W.; Kiely, C.J.; Bartley, J.K.; Hutchings, G.J. Effect on the Structure and Morphology of Vanadium Phosphates of the Addition of Alkanes during the Alcohol Reduction of $VOPO_4 \cdot 2H_2O$. *J. Mater. Chem.* **2010**, *20*, 5310–5318. [CrossRef]
16. De Farias, R.F.; Airoldi, C. Synthesis and Characterization of an $VOPO_4$-Polyaniline Lamellar Hybrid Compound. *Solid State Sci.* **2003**, *5*, 611–613. [CrossRef]
17. Borah, P.; Datta, A. Exfoliated $VOPO_4 \cdot 2H_2O$ Dispersed on Alumina as a Novel Catalyst for the Selective Oxidation of Cyclohexane. *Appl. Catal. A Gen.* **2010**, *376*, 19–24. [CrossRef]
18. Šišková, R.; Beneš, L.; Zima, V.; Vlček, M.; Votinský, J.; Kalousová, J. Redox Intercalation Reaction of Crystalline $VOPO_4 \cdot 2H_2O$ with NaI Solution in Acetone. *Polyhedron* **1993**, *12*, 181–185. [CrossRef]
19. Chauvel, A.; de Roy, M.E.; Besse, J.P.; Benarbia, A.; Legrouri, A.; Barroug, A. Redox Intercalation of Alkali Metals into Vanadyl Phosphate Dihydrate. *Mater. Chem. Phys.* **1995**, *40*, 207–211. [CrossRef]
20. Jacobson, A.J.; Johnson, J.W.; Brody, J.F.; Scanlon, J.C.; Lewandowski, J.T. Redox Intercalation Reactions of $VOPO_4 \cdot 2H_2O$ with Mono—and Divalent Cations. *Inorg. Chem.* **1985**, *24*, 1782–1787. [CrossRef]
21. Shi, H.Y.; Wu, W.; Yang, X.; Jia, Z.; Lin, Z.; Qin, Z.; Song, Y.; Guo, D.; Sun, X. Accessing the 2 V VV/VIV Redox Process of Vanadyl Phosphate Cathode for Aqueous Batteries. *J. Power Sources* **2021**, *507*, 230270. [CrossRef]
22. Ma, L.; Li, N.; Long, C.; Dong, B.; Fang, D.; Liu, Z.; Zhao, Y.; Li, X.; Fan, J.; Chen, S.; et al. Achieving Both High Voltage and High Capacity in Aqueous Zinc-Ion Battery for Record High Energy Density. *Adv. Funct. Mater.* **2019**, *29*, 1906142. [CrossRef]
23. Ma, L.; Li, Q.; Ying, Y.; Ma, F.; Chen, S.; Li, Y.; Huang, H.; Zhi, C. Toward Practical High-Areal-Capacity Aqueous Zinc-Metal Batteries: Quantifying Hydrogen Evolution and a Solid-Ion Conductor for Stable Zinc Anodes. *Adv. Mater.* **2021**, *33*, 2007406. [CrossRef] [PubMed]
24. Ma, L.; Chen, S.; Li, H.; Ruan, Z.; Tang, Z.; Liu, Z.; Wang, Z.; Huang, Y.; Pei, Z.; Zapien, J.A.; et al. Initiating a Mild Aqueous Electrolyte Co_3O_4/Zn Battery with 2.2 V-High Voltage and 5000-Cycle Lifespan by a Co(iii) Rich-Electrode. *Energy Environ. Sci.* **2018**, *11*, 2521–2530. [CrossRef]
25. Dell, R.; Rand, D.A.J. *Understanding Batteries*; Royal Society of Chemistry: Cambridge, UK, 2001.
26. Morales, D.M.; Villalobos, J.; Kazakova, M.A.; Xiao, J.; Risch, M. Nafion-Induced Reduction of Manganese and Its Impact on the Electrocatalytic Properties of a Highly Active MnFeNi Oxide for Bifunctional Oxygen Conversion. *ChemElectroChem* **2021**, *8*, 2979–2983. [CrossRef] [PubMed]
27. Marshall, J.E.; Zhenova, A.; Roberts, S.; Petchey, T.; Zhu, P.; Dancer, C.E.J.; McElroy, C.R.; Kendrick, E.; Goodship, V. On the Solubility and Stability of Polyvinylidene Fluoride. *Polymers* **2021**, *13*, 1354. [CrossRef]
28. Cholewinski, A.; Si, P.; Uceda, M.; Pope, M.; Zhao, B. Polymer Binders: Characterization and Development toward Aqueous Electrode Fabrication for Sustainability. *Polymers* **2021**, *13*, 631. [CrossRef]
29. Rietveld, H.M. A Profile Refinement Method for Nuclear and Magnetic Structures. *J. Appl. Crystallogr.* **1969**, *2*, 65–71. [CrossRef]
30. Cheary, R.W.; Coelho, A. A Fundamental Parameters Approach to X-ray Line-Profile Fitting. *J. Appl. Crystallogr.* **1992**, *25*, 109–121. [CrossRef]
31. R'Kha, C.; Vandenborre, M.T.; Livage, J.; Prost, R.; Huard, E. Spectroscopic Study of Colloidal $VOPO_4 \cdot 2H_2O$. *J. Solid State Chem.* **1986**, *63*, 202–215. [CrossRef]
32. Tietze, H.R. The Crystal and Molecular Structure of Oxovanadium(v) Orthophosphate Dihydrate, $VOPO_4 \cdot 2H_2O$. *Aust. J. Chem.* **1981**, *34*, 2035–2038. [CrossRef]
33. Antonio, M.R.; Barbour, R.L.; Blum, P.R. Interlayer Coordination Environments of Iron, Cobalt, and Nickel in Vanadyl Phosphate Dihydrate, $VOPO_4 \cdot 2H_2O$, Intercalation Compounds. *Inorg. Chem.* **1987**, *26*, 1235–1243. [CrossRef]
34. Gudarzi, M.M.; Moghadam, M.H.M.; Sharif, F. Spontaneous Exfoliation of Graphite Oxide in Polar Aprotic Solvents as the Route to Produce Graphene Oxide—Organic Solvents Liquid Crystals. *Carbon* **2013**, *64*, 403–415. [CrossRef]
35. Shpeizer, B.G.; Ouyang, X.; Heising, J.M.; Clearfield, A. Synthesis and Crystal Structure of a New Vanadyl Phosphate $[H_{0.6}(VO)_3(PO_4)_3(H_2O)_3] \cdot 4H_2O$ and Its Conversion to Porous Products. *Chem. Mater.* **2001**, *13*, 2288–2296. [CrossRef]
36. Le Bail, A. Whole Powder Pattern Decomposition Methods and Applications: A Retrospection. *Powder Diffr.* **2005**, *20*, 316. [CrossRef]
37. Jugović, D.; Milović, M.; Ivanovski, V.N.; Škapin, S.; Barudžija, T.; Mitrić, M. Microsized Fayalite Fe_2SiO_4 as Anode Material: The Structure, Electrochemical Properties and Working Mechanism. *J. Electroceramics* 2021. [CrossRef]
38. Zhao, C.; Zhang, X.; He, Z.; Guan, Q.; Li, W. Demystifying the Mechanism of NMP Ligands in Promoting Cu-Catalyzed Acetylene Hydrochlorination: Insights from a Density Functional Theory Study. *Inorg. Chem. Front.* **2020**, *7*, 3204–3216. [CrossRef]
39. Milović, M.; Vujković, M.; Jugović, D.; Mitrić, M. Electrochemical and Structural Study on Cycling Performance of Γ-LiV_2O_5 Cathode. *Ceram. Int.* **2021**, *47*, 17077–17083. [CrossRef]
40. Shannon, R.D.; Prewitt, C.T. Effective Ionic Radii in Oxides and Fluorides. *Acta Crystallogr. Sect. B Struct. Crystallogr. Cryst. Chem.* **1969**, *25*, 925–946. [CrossRef]
41. Arun, T.; Mohanty, A.; Rosenkranz, A.; Wang, B.; Yu, J.; Morel, M.J.; Udayabhaskar, R.; Hevia, S.A.; Akbari-Fakhrabadi, A.; Mangalaraja, R.V.; et al. Role of Electrolytes on the Electrochemical Characteristics of Fe_3O_4/MXene/RGO Composites for Supercapacitor Applications. *Electrochim. Acta* **2021**, *367*, 137473. [CrossRef]
42. Iqbal, M.Z.; Zakar, S.; Haider, S.S. Role of Aqueous Electrolytes on the Performance of Electrochemical Energy Storage Device. *J. Electroanal. Chem.* **2020**, *858*, 113793. [CrossRef]